Improved optimal fingerprinting based on estimating equations reaffirms anthropogenic effect on global warming

Yan Li, Tianying Wang, Jun Yan, and Xuebin Zhang

2025

Improved Optimal Fingerprinting Based on Estimating Equations Reaffirms Anthropogenic Effect on Global Warming

YAN LI,[a] TIANYING WANG,[b] JUN YAN,[c] AND XUEBIN ZHANG[d]

[a] *Department of Mathematics and Statistics, Auburn University, Auburn, Alabama*
[b] *Department of Statistics, Colorado State University, Fort Collins, Colorado*
[c] *Department of Statistics, University of Connecticut, Storrs, Connecticut*
[d] *Pacific Climate Impacts Consortium, University of Victoria, Victoria, British Columbia, Canada*

(Manuscript received 6 April 2024, in final form 25 November 2024, accepted 18 December 2024)

ABSTRACT: The optimal fingerprinting approach is central to detecting and attributing climate change. It utilizes a regression model with covariates that have measurement errors, linked by a shared covariance matrix with the regression error up to a known scale. The inferences about the regression coefficients are vital for making reliable detection and attribution statements, as well as for quantifying uncertainties in outcomes like attributable warming. Traditionally, this has involved the total least squares (TLS) method, which depends on accurately estimating the covariance matrix of the regression error. However, inaccuracies in this matrix's estimation can lead to skewed scaling factor estimators and overly optimistic confidence intervals, potentially misrepresenting the accuracy of detection and attribution statements. The recent advent of an estimating equations approach, which offers more efficient point estimation with smaller possible variance and precise uncertainty quantification, prompts a critical reassessment of past climate change detection and attribution analyses. By applying this advanced method to HadCRUT5 observational data and CMIP6 multimodel simulations, our study reevaluates temperature detection and attribution at global and regional levels, strengthens the existing detection and attribution conclusions at the global scale, and provides evidence of the effect of anthropogenic forcings in various regions.

SIGNIFICANCE STATEMENT: Optimal fingerprinting plays an essential role in quantifying human impacts on climate change by facilitating the statistical analysis of estimated scaling factors, which is fundamental for detecting and attributing climate change to external forces. A well-acknowledged challenge in this process is the estimation of the covariance matrix of the regression error, which is critical in correcting the bias due to errors in variables and quantifying the uncertainty of the resulting estimator. The challenge remained unsolved until the recent advancement of an estimating equations approach, which ensures efficient unbiased point estimators and reliable confidence intervals. Using this method, this work reassesses the previous climate change detection and attribution studies with the latest datasets, HadCRUT5 and CMIP6. This reevaluation confirms earlier findings on the global scale and unveils human impacts in various regions.

KEYWORDS: Climate change; Error analysis; Numerical analysis/modeling; Anthropogenic effects/forcing

1. Introduction

Optimal fingerprinting stands as the predominant technique for climate change detection and attribution (e.g., Hasselmann 1997; Allen and Stott 2003; Hegerl et al. 2010). This method involves a regression analysis where the observed climate variable of interest is regressed on expected changes of the climate system, known as "fingerprints," in response to certain external forcings. The essence of this approach depends on inferences about the regression coefficients, often termed scaling factors, which adapt the climate-model-predicted fingerprints to align with the observed climate changes. The term "optimal" originally referred to the application of generalized least squares (GLS), optimized when the weight matrix is chosen to be the precision matrix of the regression error to yield minimum variance of the scaling factor estimator. Although it has become clear that optimal is a misnomer since the GLS setting does not apply because the covariance matrix of the regression error is estimated (Li et al. 2023b), the term "optimal fingerprinting" continues to be used in the literature for historical reasons. We refer to it as simply fingerprinting for accuracy.

The regression model in fingerprinting has two special features that differentiate it from standard regressions. First, the regressors—fingerprints of external forcings—are not observed but estimated from climate model simulations, leading to an errors-in-variables (EIV) problem that can affect the accuracy of regression coefficients and the reliability of confidence intervals. The total least squares (TLS) method, as proposed in Allen and Stott (2003), addresses this by "prewhitening" both response and predictors with the regression error's covariance matrix, separately estimated from preindustrial simulations (e.g., Ribes et al. 2013; Hannart et al. 2014). Second, the regression error's covariance matrix, crucial for prewhitening in TLS, exhibits spatiotemporal dependence. Accurately estimating this matrix is challenging due to the sparse availability of climate model simulations relative to

Corresponding author: Tianying Wang, tianying.wang@colostate.edu

DOI: 10.1175/JCLI-D-24-0193.1

the matrix's high dimensionality. Techniques have evolved from projecting data onto empirical orthogonal functions (EOFs) (Hegerl et al. 1996; Allen and Tett 1999) to employing regularized optimal fingerprinting (ROF) with a linear shrinkage estimator for the covariance matrix estimation (Ribes et al. 2009; Ledoit and Wolf 2004), significantly enhancing the method's precision (Ribes et al. 2013).

Recent investigations have revealed the detrimental effects of relying on estimated, often imprecise, error covariance matrices for scaling factor estimations in fingerprinting. The resulting point estimators are not optimal in terms of mean-square error (Li et al. 2023b). The confidence intervals are overly narrow to cover the true scaling factors with their nominal confidence levels (DelSole et al. 2019; Li et al. 2021). While the integrated optimal fingerprinting method (Hannart 2016) addresses EIV and covariance matrix uncertainties with an inverse-Wishart prior, it is not practical due to the highly informative prior. The parametric bootstrap method for improved confidence interval coverage (Li et al. 2021) shows constrained effectiveness with sparse data. Conversely, the estimating equations (EE) method introduced by Ma et al. (2023) presents a novel solution, offering unbiased estimators that adjust for EIV bias and utilize the error covariance matrix structure for more precise weight construction. This method, assuming temporal stationarity in climate variability, incorporates a pseudobootstrap algorithm for interval estimation, yielding estimators and confidence intervals with enhanced efficiency and closer-to-nominal coverage rates, surpassing the ROF's performance.

With the advent of the estimating equations approach, a reassessment of previous climate change detection and attribution findings derived from potentially imprecise methodologies becomes imperative. As the analyses and conclusions in the recent IPCC assessment report (Eyring et al. 2021) were obtained based on ROF, an urgent and pertinent question then emerges: How would the use of refined confidence intervals from the EE approach impact the conclusions of existing detection and attribution studies? From the substantive climate science aspect, we applied the EE approach, which addresses the limitations of prevailing approaches in the existing literature, to systematically evaluate the evidence of human influence on surface temperature at both the global and regional scales with the latest HadCRUT5 observational data (Morice et al. 2021) and CMIP6 multimodel simulations (Eyring et al. 2016). At the global scale, we reexamined the analyses of global mean temperature conducted by Gillett et al. (2021), which used ROF and a multimodel mean approach, and assessed the results in comparison with those from the EE approach. To differentiate human impacts on climate across different regions, we carried out both two-signal and three-signal analyses at multiple regional scales as defined in the latest IPCC Sixth Assessment Report (AR6) (Iturbide et al. 2020), and such systematic regional analysis was not available at the time of the AR6 assessment (Gutiérrez et al. 2021). Our analysis benefits the detection and attribution community with the reevaluation of existing results using the latest methods and data, strengthens the existing detection and attribution conclusions at the global scale, and provides evidence of the effect of anthropogenic forcings at various regions.

The remainder of this paper is structured as follows. Section 2 provides an overview of the EE approach, with more specifics available in the appendix. In section 3, we detail the data utilized in our study, encompassing observational data, outputs from climate models under external forcings, and preindustrial control runs. Our findings, in comparison with the recent study of Gillett et al. (2021), are presented in section 4, followed by a discussion in section 5. Additionally, for practical application, we have made the implementation of both the EE and ROF approaches accessible through the open-source R package dacc (Li et al. 2023a).

2. Method overview

We consider the data with T time periods and S spatial regions or sites. At the time period $t = 1, \ldots, T$ and site $s = 1, \ldots, S$, we denote the observed climate variable as Y_{ts}, the unobserved expected climate response to the jth external forcing as X_{tsj} for $j = 1, \ldots, J$, and the observed climate response under the jth external forcing, which is the average of m_i climate model simulations, as $\tilde{X}_{tsj}$. For ease of representation, we denote $Y_t = (Y_{t1},\ldots,Y_{ts})^\top \in \mathbb{R}^S$, $X_{tj} = (X_{t1j},\ldots,X_{tSj})^\top \in \mathbb{R}^S$, and $\tilde{X}_{tj} = (\tilde{X}_{t1j},\ldots,\tilde{X}_{tSj})^\top \in \mathbb{R}^S$. For a time point t, the optimal fingerprinting takes the form of a linear regression with errors in variables (Ribes et al. 2013):

$$\begin{cases} Y_t = \sum_{j=1}^{J} X_{tj}\beta_j + \boldsymbol{\epsilon}_t, \\ \tilde{X}_{tj} = X_{tj} + \nu_{tj}, \qquad j = 1, \ldots, J, \end{cases} \tag{1}$$

where β_j is the unknown scaling factor to the jth external forcing, $\boldsymbol{\epsilon}_t = (e_{t1},\ldots,e_{ts})^\top$ is the vector of regression errors, and $\boldsymbol{\nu}_{tj} = (\nu_{t1j}, \ldots, \nu_{tSj})$ is the vector of measurement error in estimating X_{tj} with $\tilde{X}_{tj}$ at the time period t. No intercept is present because the outcome and the signals are both centered on the same reference level.

The internal variation of the climate system and the variation of the climate model simulations are reflected in the covariance matrix of the regression error and the measurement error in model (1). Let $\boldsymbol{\epsilon} = (\boldsymbol{\epsilon}_1^\top,\ldots,\boldsymbol{\epsilon}_T^\top)^\top \in \mathbb{R}^{ST}$ and $\nu_j = (\nu_{1j}^\top,\ldots,\nu^\top)^\top \in \mathbb{R}^{ST}$ for $j = 1, \ldots, J$. The errors $\boldsymbol{\epsilon}$ and $\nu_1, \ldots, \nu_J$ are assumed to be mutually independent, with zero mean and covariance matrices $\boldsymbol{\Sigma}$, $\boldsymbol{\Omega}_1, \ldots,$ and $\boldsymbol{\Omega}_J$, respectively. Since the climate models are assumed to reflect the same internal variability as the climate system, we have $\boldsymbol{\Omega}_j = \boldsymbol{\Sigma}/m_j$, where m_j is the number of available runs for the jth forcing. In the EE approach proposed by Ma et al. (2023), this assumption is relaxed to allow climate model simulations to have the same pattern but a different scale than the internal climate system variability (i.e., $\boldsymbol{\Omega}_j = a\boldsymbol{\Sigma}/m_j$; see assumption 2 of Ma et al. 2023). A more detailed discussion about the scale parameter a, related model assessments, and potential future improvements is provided in section 5.

The true $\boldsymbol{\Sigma}$ is typically unknown with a spatially and temporally dependent structure and needs to be estimated by utilizing a set of independent control runs of size L that reflects the

climate's natural internal variability, denoted as $\{\boldsymbol{\epsilon}^{(1)}, \ldots, \boldsymbol{\epsilon}^{(L)}\}$. A reliable estimate of the matrix $\boldsymbol{\Sigma}$ requires the size L to be much greater than $S \times T$. The reality is, however, that the sample size is often very small relative to the dimension, in which case, the sample covariance is not even of full rank and thus not invertible. Various methods have been proposed to improve the estimation, including the use of a regularized estimator to ensure the positive definiteness of the weight matrix (Ribes et al. 2013). The point estimation of the parameter of interest β_j in Eq. (1) is then commonly estimated from ROF with the estimated regularized weight matrix. The corresponding confidence intervals can be constructed from the normal approximation (Ribes et al. 2013; DelSole et al. 2019; Li et al. 2021) or bootstrap approach (Pesta 2013; DelSole et al. 2019).

To tackle the point and interval estimations for the scaling factors in the optimal fingerprinting regression with an unknown covariance matrix, Ma et al. (2023) recently proposed an efficient, bias-corrected EE approach with less restrictive model assumptions on the structure of true covariance matrices $\boldsymbol{\Sigma}$ and $\boldsymbol{\Omega}_J$ than the ROF approach with TLS, which has been proven to provide valid and efficient confidence intervals for the scaling factors with close-to-nominal coverage rates.

More specifically, the EE method incorporates a scale parameter in the covariance matrices to account for the proportion of variances among different climate simulation models. That is, it is assumed that there is a scale parameter $a > 0$ such that $\boldsymbol{\Omega}_j = a\boldsymbol{\Sigma}/m_j$, $J = 1, \ldots, J$, and the shared covariance matrix of the control runs $\boldsymbol{\epsilon}^{(\ell)}s$ is $\boldsymbol{\Psi} = a\boldsymbol{\Sigma}$. The point estimator and confidence intervals for a are also provided for model diagnostics, detailed in Ma et al. (2023). Typical ROF-approach-based applications usually assume $a = 1$ and use a residual consistency test for validation. By adding an extra scale, the EE approach provides additional flexibility and is capable of handling more general cases of detection and attribution analysis. Moreover, in the case studies of the HadCRUT4 (Morice et al. 2012) and CanESM5 (Swart et al. 2019) data of Ma et al. (2023), the estimated scale parameter $\hat{a}$ varies across different sites, and rigorous hypothesis testing suggests that the common assumption required in OF (i.e., H_0: $a = 1$) is invalid in many regions.

In addition, the EE method assumes that the internal climate variability does not change over time; i.e., it is temporally stationary, which is not a typical assumption in ROF in an explicit way. Nonetheless, in practice, the estimation of $\boldsymbol{\Sigma}$ does not consider temporal changes, and there is no evidence that the variance changes on the time and space scales. Therefore, the EE only utilizes diagonal blocks of the estimated covariance matrices $\hat{\boldsymbol{\Sigma}}$ and $\hat{\boldsymbol{\Omega}}$ in the point estimator of the scaling factor without specifying the off-diagonal blocks that capture the temporal dependence across time. In other words, no assumptions of parametric forms are imposed on the off-diagonal blocks, which are not necessarily zero but do not need to be estimated. The temporal stationarity assumption greatly reduces the number of parameters in $\boldsymbol{\Sigma}$. This assumption implies that the covariance matrix $\boldsymbol{\epsilon}_t$ and $\boldsymbol{\epsilon}_{t'}$ depend only on the time lag $|t - t'|$. Consequently, the $TS \times TS$ covariance matrix of the stacked error vector $\boldsymbol{\epsilon}$ is block Toeplitz. The point estimation uses only the diagonal blocks, discarding the information in the off-diagonal blocks. In Ma et al. (2023), it has been shown to be more efficient than the TLS approach. This can be explained by the fact that, while the EE method loses some efficiency in point estimation by not estimating the temporal correlation, it gains efficiency by providing a much more reliable estimator of a suboptimal weight matrix. In contrast, traditional fingerprinting methods use the full space–time covariance for the highest efficiency but can be compromised by the large uncertainty in estimating this high-dimensional covariance. When constructing the confidence intervals for the scaling factor of interest, a pseudobootstrap algorithm, which uses control runs to create pseudocopies of residuals, has been developed to properly account for the unspecified temporal dependency. More details of the pseudobootstrap method are presented in the appendix.

3. Data preparation

In this study, we undertook a detection and attribution analysis of annual-mean near-surface air temperatures on both global and regional scales for the period 1951–2020. The analyses utilized the latest HadCRUT5 observational data (Morice et al. 2021) and CMIP6 multimodel simulations (Eyring et al. 2016). On the regional scale, the analyses were done on the 43 subcontinental regions as defined in the Working Group 1 (WGI) contribution to the IPCC Sixth Assessment Report (Iturbide et al. 2020), illustrated in Fig. 1. However, due to extensive missing observations, the East Antarctica (EAN) and West Antarctica (WAN) regions were excluded. Additionally, three South American regions such as southern South America (SSA), southwestern South America (SWS), and northwest South America (NWS) were omitted owing to unstable estimation results in these areas.

For each analysis, model (1) requires three components: (i) the vector of observed mean temperatures, denoted as $Y = (Y_1^\top, \ldots, Y_T^\top)^\top$; (ii) the estimated fingerprints $\tilde{X}_j = (\tilde{X}_{1j}^\top, \ldots, \tilde{X}_{Tj}^\top)^\top$, derived from climate model simulations under the jth external forcing, $J = 1, \ldots, J$; and (iii) control runs, represented by $\boldsymbol{\epsilon}^{(1)}, \ldots, \boldsymbol{\epsilon}^{(L)}$, from climate model simulations, which are crucial for estimating the covariance matrix $\boldsymbol{\Sigma}$. Detailed descriptions of the data for each of these components are provided as follows.

a. Observed temperature anomalies

While the analysis conducted by Gillett et al. (2021) chose the global mean temperature anomalies from HadCRUT4 relative to the preindustrial base period 1850–1900, we obtained the annual means of observed temperature anomalies from the latest HadCRUT5 datasets (Morice et al. 2021) for the period of 1951–2020. Compared to the HadCRUT4, the HadCRUT5 dataset is expected to be around 0.1° warmer for much of the past 50 years, and up to 0.2° in recent years due to corrections of bias in measurement techniques, which is confirmed in our later analysis of attributable warming.

The raw data were monthly temperature anomalies relative to the average over a 1961–90 reference period in near-surface air temperature from January 1850, measured across 5° × 5° grid

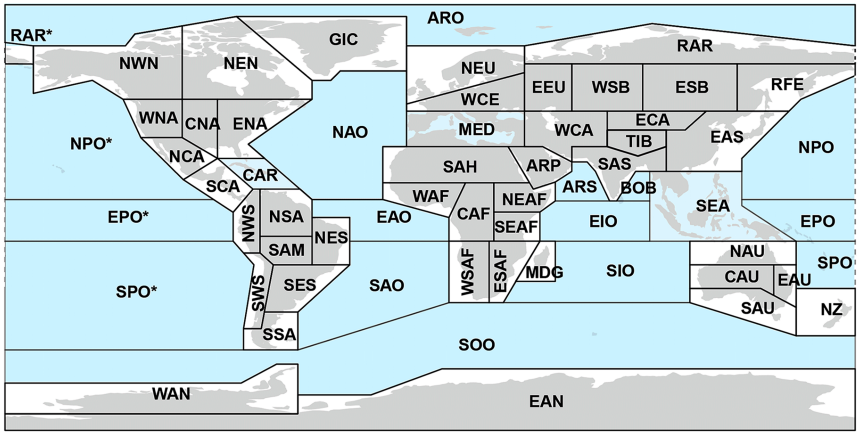

1	GIC	Greenland/Iceland	23	SAH	Sahara	43	NAU	N.Australia
2	NWN	N.W.North-America	24	WAF	Western-Africa	44	CAU	C.Australia
3	NEN	N.E.North-America	25	CAF	Central-Africa	45	EAU	E.Australia
4	WNA	W.North-America	26	NEAF	N.Eastern-Africa	46	SAU	S.Australia
5	CNA	C.North-America	27	SEAF	S.Eastern-Africa	47	NZ	New-Zealand
6	ENA	E.North-America	28	WSAF	W.Southern-Africa	48	EAN	E.Antarctica
7	NCA	N.Central-America	29	ESAF	E.Southern-Africa	49	WAN	W.Antarctica
8	SCA	S.Central-America	30	MDG	Madagascar	50	ARO	Arctic-Ocean
9-10	CAR	Caribbean	31	RAR	Russian-Arctic	51	NPO	N.Pacific-Ocean
11	NWS	N.W.South-America	32	WSB	W.Siberia	52	EPO	Equatorial.Pacific-Ocean
12	NSA	N.South-America	33	ESB	E.Siberia	53	SPO	S.Pacific-Ocean
13	NES	N.E.South-America	34	RFE	Russian-Far-East	54	NAO	N.Atlantic-Ocean
14	SAM	South-American-Monsoon	35	WCA	W.C.Asia	55	EAO	Equatorial.Atlantic-Ocean
15	SWS	S.W.South-America	36	ECA	E.C.Asia	56	SAO	S.Atlantic-Ocean
16	SES	S.E.South-America	37	TIB	Tibetan-Plateau	57	ARS	Arabian-Sea
17	SSA	S.South-America	38	EAS	E.Asia	58	BOB	Bay-of-Bengal
18	NEU	N.Europe	39	ARP	Arabian-Peninsula	59	EIO	Equatorial.Indic-Ocean
19	WCE	Western&Central-Europe	40	SAS	S.Asia	60	SIO	S.Indic-Ocean
20	EEU	E.Europe	41-42	SEA	S.E.Asia	61	SOO	Southern-Ocean
21-22	MED	Mediterranean						

FIG. 1. Boundaries of IPCC AR6 WGI reference regions sourced from Iturbide et al. (2020).

boxes. At each grid box, annual-mean temperatures were computed from these monthly temperatures provided at least 9 months of data were in a given year; otherwise, the annual mean for that year was marked as missing. Subsequently, in the same practice as Gillett et al. (2021), 5-yr averages were computed, requiring no more than two annual averages to be missing. This yielded up to 14 values of 5-yr averages per grid box. For the analysis on the global scale, the 5° × 5° grid boxes were aggregated with area weighting into larger 40° × 30° grid boxes to reduce the spatial dimension (Zhang et al. 2006). That is, the regional mean over all available 5° grid boxes was computed for each of the 40° × 30° grid boxes. It is important to note that the EE method does not strictly require such dimension reduction; analyses can be performed directly on the original 5° grid boxes. However, doing so increases the estimation variance and decreases the efficiency of the EE approach, as well as any other methods with an estimated prewhitening matrix. In fact, traditional fingerprinting techniques, which rely on estimating the full spatiotemporal covariance, would be further compromised by the enlarged dimension of the covariance matrix. The regional analyses were done on the original 5° × 5° grid boxes defined by the HadCRUT5 dataset. Table 1 presents a summary of the spatiotemporal dimensions, specifically the number of grid boxes and time steps, as well as the total count of observations retained after the exclusion of missing values for both global and regional analyses.

b. *Climate model simulations under external forcings*

Three external forcings were considered using outputs from CMIP6 models for the selected period of 1951–2020, encompassing simulations for hist-GHG (driven exclusively by changes in well-mixed greenhouse gas concentrations), hist-aer (driven exclusively by changes in anthropogenic aerosol emissions and burdens), and hist-nat (driven exclusively by natural forcings). The details of the climate model simulations are summarized in Table 2. The hist-ALL (driven by changes in all anthropogenic and natural forcings) simulations from historical ensembles are only available up to the year 2014 for the CMIP6 models listed in Table 2. Therefore, instead of using the hist-ALL simulations for the regressions by model (1) and then deriving the regression coefficients corresponding to anthropogenic or combined greenhouse gas forcings as in Allen and Tett (1999) or Gillett et al. (2021), we first consider a three-signal regression analysis to directly quantify the contribution of individual forcings, including aerosols (AERs; inferred from hist-aer), greenhouse gases (GHG; inferred from hist-GHG), and natural (NAT) forcings (inferred from hist-nat).

In the three-signal regression analyses, each of the climate model simulation outputs is treated in the same way as we

TABLE 1. Summaries of names, ideal spatiotemporal dimensions (S and $T = 13$), and dimension of observation N after removing missing values of the 44 regions analyzed in the study.

Acronym	Regions	Grid size (1° × 1°)	S	N
GL	Global	40 × 30	54	696
	Subcontinental regions			
ARP	Arabian Peninsula	5 × 5	11	143
CAF	Central Africa	5 × 5	14	182
CAU	Central Australia	5 × 5	14	182
CNA	Central North America	5 × 5	13	169
EAS	East Asia	5 × 5	35	455
EAU	East Australia	5 × 5	6	78
ECA	Eastern central Asia	5 × 5	15	195
EEU	East Europe	5 × 5	16	208
ENA	Eastern North America	5 × 5	23	299
ESAF	Eastern and southern Africa	5 × 5	14	182
ESB	East Siberia	5 × 5	32	416
GIC	Greenland/Iceland	5 × 5	57	741
MDG	Madagascar	5 × 5	8	104
NAU	North Australia	5 × 5	18	234
NCA	North and Central America	5 × 5	11	143
NEAF	Northeastern Africa	5 × 5	16	208
NEN	Northeast North America	5 × 5	58	754
NES	Northeast South America	5 × 5	12	156
NEU	North Europe	5 × 5	40	520
NSA	Northern South America	5 × 5	16	208
NWN	Northwest North America	5 × 5	61	793
NZ	New Zealand	5 × 5	20	260
RAR	Russian Arctic	5 × 5	74	962
RFE	Russian Far East	5 × 5	31	403
SAH	Sahara	5 × 5	34	442
SAM	South American monsoon	5 × 5	8	104
SAS	South Asia	5 × 5	19	247
SAU	South Australia	5 × 5	22	286
SCA	South and Central America	5 × 5	13	169
SEAF	Southeastern Africa	5 × 5	8	104
SES	Southeast South America	5 × 5	19	247
TIB	Tibetan Plateau	5 × 5	6	78
WAF	Western Africa	5 × 5	15	195
WCA	West and central Asia	5 × 5	23	299
WCE	West and central Europe	5 × 5	20	260
WNA	Western North America	5 × 5	13	169
WSAF	West South Africa	5 × 5	15	195
WSB	West Siberia	5 × 5	24	312

obtain the observed temperature anomalies from HadCRUT5. The missing pattern in Y was used to mask the simulated data to match the two. Then, in order to maintain the same spatiotemporal structure, annual anomalies for each grid box were computed by centering with the average of observed annual temperatures over 1961–90, consistent with the procedure used by HadCRUT5. The same procedure of 5-yr average and gridbox aggregation used in preparing Y was applied to each simulation run. The final estimated fingerprints $\tilde{X}_j$ were then computed as averages over all available runs across all available models and ensemble members, giving equal weight to each model. The climate model effects are discarded as in Zhang et al. (2006) and Wan et al. (2019). This preprocessing results in the same spatiotemporal dimensions for each regional dataset.

TABLE 2. List of CMIP6 ensembles of simulations used to estimate the fingerprint of external forcings. Total numbers for the forcings are 43, 43, and 40 for GHG, AER, and NAT, respectively.

Model	Ensemble	No. of runs
BCC-CSM2-MR	hist-GHG	3
	hist-aer	3
	hist-nat	3
CanESM5	hist-GHG	10
	hist-aer	10
	hist-nat	10
CNRM	hist-GHG	10
	hist-aer	10
	hist-nat	10
HadGEM3	hist-GHG	4
	hist-nat	4
IPSL	hist-GHG	10
	hist-aer	10
	hist-nat	10
MIROC6	hist-GHG	3
	hist-aer	3
MRI-ESM2	hist-GHG	3
	hist-aer	3
	hist-nat	3
NorESM2	hist-aer	3

As for the two-signal analysis of anthropogenic (ANT) and NAT forcings, with the assumption of linear additivity $X_{\mathrm{ANT}} = X_{\mathrm{GHG}} + X_{\mathrm{AER}}$ (Tett et al. 2002; Zhang et al. 2006; Wan et al. 2019), we obtain for each model the fingerprints of ANT by combining fingerprints of the aerosols and greenhouse gas forcings.

More specifically, for the fingerprint of ANT forcings, we first consider each individual of the CMIP6 models listed in Table 2. Within each model, if the model simulations for hist-GHG and hist-aer are both presented and under the same configurations, we compute the model averages for the responses to the two GHG and AER forcings and then combine the calculated means to construct the responses for ANT forcings of the corresponding model. For instance, for the Beijing Climate Center (BCC) climate system model in Table 2, three different simulation runs are obtained for both hist-GHG and hist-aer indexed by ensemble extension r1i1p1f1, r2i1p1f1, and r3i1p1f1, implying the same initialization, perturbation, and forcing conditions across all members of ensemble. This allows us to easily splice together the appropriate runs to construct the climate responses to ANT forcings. Then, the final estimated fingerprints for ANT $\tilde{X}_{\mathrm{ANT}}$ used in model (1) are computed as the multimodel average. The equivalent sample size m_{ANT} is computed accordingly based on the number of runs for GHG and AER forcings in each model and the total number of models.

c. *Preindustrial control runs*

Estimation of $\mathbf{\Sigma}$ was based on $L = 181$ runs of 70 years constructed from 29 preindustrial control simulations of various

TABLE 3. List of CMIP6 control simulations used to estimate the internal climate variability. Number of replicates indicates the number of nonoverlapping blocks of 70-yr segments taken from the model simulations.

Model	No. of replicates
AWI-CM-1-1-MR	7
BCC-CSM2-MR	8
BCC-ESM1	6
CAMS-CSM1-0	7
CNRM-CM6-1	7
CNRM-ESM2-1	7
EC-EARTH3	7
EC-EARTH3-Veg	7
FIO-ESM-2-0	5
GFDL CM4	7
GFDL-ESM4	7
GISS-E2-1-G (r101)	2
GISS-E2-1-G (r102)	2
GISS-E2-1-G (r1f1)	12
GISS-E2-1-G (r1f2)	4
GISS-E2.1-G (r1f3)	1
GISS-E2.1-G (r2f1)	1
GISS-E2.1-G-CC	2
GISS-E2.1-H	11
HadGEM3-GC3.1-LL	7
HadGEM3-GC3.1-MM	7
IPSL-CM6A-LR (r1i1)	17
IPSL-CM6A-LR (r1i2)	3
NorCPM1 (r1)	7
NorCPM1 (r2)	7
NorCPM1 (r3)	7
NorESM1-F	2
NorESM2-LM	4
UKESM1-0-LL	10
Total	181

lengths of years, obtained from global climate models participating in CMIP6 multimodel ensembles. The multimodel estimate of $\mathbf{\Sigma}$ has lower sampling variability than individual model estimates. The time periods of control simulations vary from 100 to 1200 years. The long-term linear trend was removed separately from the control simulations at each grid point to remove model drift. As $\mathbf{\Sigma}$ is assumed to be stationary over time, each control simulation was split into nonoverlapping blocks of 70 years. Then, each 70-yr block was masked by the same missing pattern as the HadCRUT5 data to create up to 14 5-yr averages at each grid box, resulting in 181 runs to estimate $\mathbf{\Sigma}$. The number of simulations available from different preindustrial control simulations that are used in the estimation of the $\mathbf{\Sigma}$ is summarized in Table 3.

4. Results

In this study, we first revisited the detection and attribution analyses to assess the contributions of individual forcings to the observed global temperature trend, following the processing methodology outlined by Gillett et al. (2021), using the latest HadCRUT5 dataset and the CMIP6 multimodel simulations. While our approach mirrored that of Gillett et al. (2021), who utilized the earlier HadCRUT4 dataset, we anticipate that the findings from the current dataset will offer enhanced robustness and shed some new insights, stemming from corrections for biases observed in recent years within the HadCRUT5 data.

Figure 2a presents the estimated scaling factors and their 90% confidence intervals for responses to ANT and NAT forcings. We compare three sets of results: 1) those derived from the EE approach; 2) results using the two-sample (TS) ROF method with HadCRUT5 data, as outlined by Gillett et al. (2021); and 3) findings from Gillett et al. (2021) and the AR6, based on HadCRUT4 data. The alignment of EE with AR6 results supports prior conclusions that the anthropogenic response is detectable as the confidence interval of ANT is above zero, and the anthropogenic response of the multimodel average is of realistic magnitude as observed in real-world response by the fact of the estimated confidence interval being around unity 1. The NAT forcing remained undetected, consistent with the findings of Gillett et al. (2021). Nonetheless, notable differences are observed in the point estimates and confidence intervals of the scaling factors, suggesting variability across methodologies and datasets.

To exclude discrepancies from different HadCRUT data versions and gridbox scales, we compared the EE and TS method results using the same HadCRUT5 dataset and CMIP6 simulations, focusing on scaling factor consistency across methodologies. The EE and TS methods yielded closely aligned point estimates, suggesting robustness in the estimation of scaling factors. A notable distinction, however, is in the confidence intervals; the TS method produced consistently narrower intervals across all forcings, even suggesting the detectability of NAT forcings. This discrepancy could lead to divergent conclusions, despite AR6's consistent findings. The findings, in line with Ma et al. (2023), reflect the classical ROF and EE approach's inherent characteristics, as elaborated in Ma et al. (2023). Specifically, the TS ROF method is prone to underestimation of the uncertainty of the scaling factor estimates, which results in shorter confidence intervals with lower confidence level, as indicated by the shorter confidence intervals of the TS approach compared to those of the EE approach. On the other hand, the TS ROF method has lower efficiency than the EE method, i.e., significantly larger mean-square error (MSE) in the estimation of the scaling factors, which means the location of the confidence intervals has a wider range than that of the EE method. The joint impacts of underestimated uncertainty and less-efficient point estimators may lead to divergent paradoxical outcomes: either correct detection conclusions with less reliable uncertainty measures or falsely detected external forcings.

Next, we conducted a three-signal analysis with GHG, AER, and NAT forcings to assess their separate contribution to observed temperature changes. The estimated scaling factors and their corresponding confidence intervals for this analysis are illustrated in Fig. 2b. The detection conclusions are consistent with the findings of Gillett et al. (2021), and our analysis of the EE approach also supports the detectability of GHG and AER contributions, with both factors demonstrating realistic magnitudes, i.e., regression coefficients varying

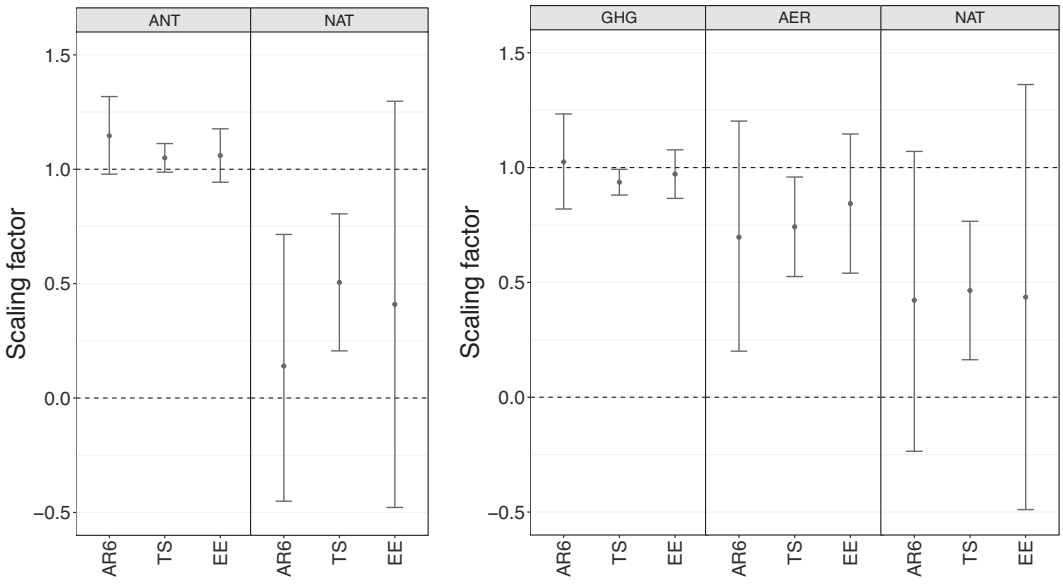

FIG. 2. Estimated signal scaling factors required to best match observed 1950–2020 annual-mean temperature on a global scale. (from left to right) The two panels show results for the two-signal and three-signal analyses, respectively. The scaling factors and corresponding 90% confidence intervals are obtained from ROF method outputs from Gillett et al. (2021) (AR6), the same two-sample ROF method as in Gillett et al. (2021) (TS), and the newly proposed EE approach (EE) using the latest HadCRUT5 and CMIP6 datasets.

around unity. Nonetheless, using the TS approach revealed that the responses to AER forcings were significantly overestimated. The observed disparities in the lengths of confidence intervals between the EE and TS approaches are consistent with those noted in our two-signal analysis, further reinforcing our claim that the existing detection and attribution analyses might lead to paradoxical conclusions due to unreliable estimates of confidence intervals. As for the noticeable discrepancy between the outcomes derived from the TS and AR6, it might be attributed to different CMIP6 model simulations. Specifically, our analysis utilized responses from eight CMIP6 models, as detailed in Table 2, in contrast to AR6, which synthesized results from an ensemble of 13 climate models. Among these, several models demonstrated significantly larger internal climate variability, leading to less reliable scaling factor estimates with wide confidence intervals.

We have also quantified the attributable warming in the global mean temperature in 2010–20 relative to the selected year period 1850–1900 by mimicking the analysis of Gillett et al. (2021). More specifically, the estimates of attributable warming of different forcings were calculated in the following steps. For each of the considered forcings, ANT, NAT, GHG, and AER, we first compute the average over the year 2010–20 for the global mean near-surface air temperature responses to the corresponding forcing; then, the temperature changes relative to the average of a preindustrial period 1850–1900 are calculated for each of those forcings. We then multiply the warming changes by the corresponding estimated regression coefficients to get the attributable warming. The calculation of attributable warming incorporates the uncertainties from two main sources: the scaling factor estimates and the simulated responses to individual forcings in CMIP6 models. Both types of uncertainties were rigorously considered in establishing the confidence ranges for the attributable warming, adhering to the approach outlined by Gillett et al. (2021).

Our analysis showed that anthropogenic forcings have contributed to 1.01°–1.25°C of warming in global mean near-surface air temperature in recent years, relative to preindustrial levels. This finding is consistent with an observed warming of 1.21°C. When compared to the range of 1.01°–1.40°C in attributable warming of ANT forcings from Gillett et al. (2021) using HadCRUT5 and multimodel simulations, our estimated range for anthropogenic warming suggests enhanced robustness and reliability. This improvement can be attributed to the efficiency and bias corrections implemented in the EE approach, in contrast to the classical ROF method. Furthermore, our three-signal analysis showed that the greenhouse gases and aerosols contributed changes from 1.70° to 2.11°C and from −0.89° to −0.42°C, respectively, and natural forcings contributed changes from −0.03° to 0.08°C. These results, from both two-signal and three-signal analyses, present a comparable pattern of attributable warming by different forcings than those reported in Gillett et al. (2021), underscoring the consistency of our findings with established research while highlighting the precision brought forth by our methodological enhancements.

We extended our detection and attribution analyses to various AR6 regions utilizing the EE approach for enhanced efficiency and reliability. Our regional analysis, based on the continental and subcontinental regions defined by Morice et al. (2021), unveiled novel insights that have not been previously explored in the existing literature.

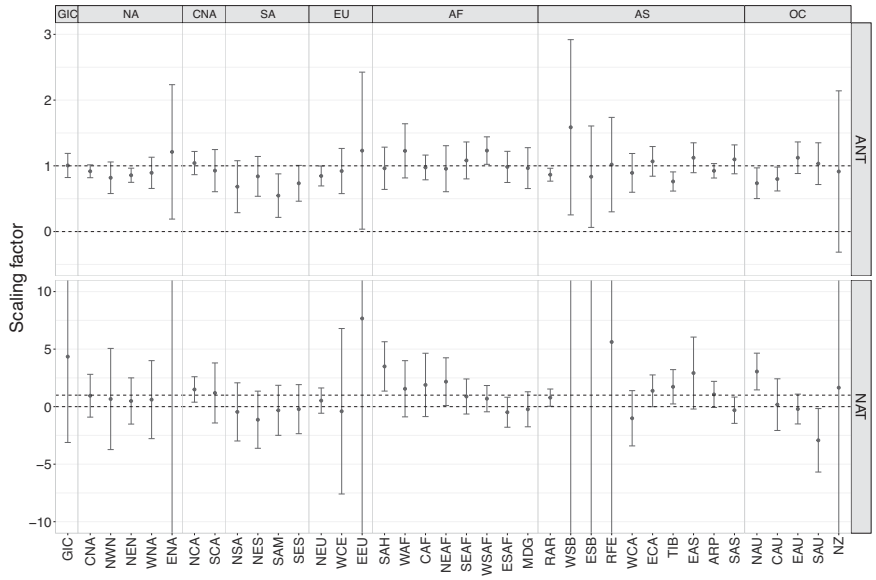

FIG. 3. Estimated signal scaling factors required to best match observed 1950–2020 annual-mean temperature for different regional domains. (from top to bottom) The two panels show results for the two-signal analysis. 90% confidence intervals are constructed from the EE approach. The longest few intervals for the NAT scaling factor are cropped to improve visualization.

Figure 3 displays the results from the two-signal analysis assessing the impacts of ANT and NAT forcings. An attributable ANT forcing effect was consistently observed across a wide range of regions. Notably, New Zealand (NZ) in Oceania emerged as an exception where this effect was not evident. Additionally, the confidence intervals for the majority of regions encompassed the value of unity (1), indicating that, on an average scale, the simulated responses to ANT forcing align with observed temperature patterns. In contrast, NAT forcing remained largely undetected, except in specific regions including North Central America (NCA) around Mexico, the Sahara (SAH) region, and North Australia, highlighting regional sensitivities to natural climatic variability.

However, it is noticeable that our results suggest that the responses to ANT are significantly overestimated for regions, including northeastern North America (NEN), South American monsoon (SAM), Russian Arctic (RAR), and Tibetan Plateau (TIB). Previous work suggested that those regions are sensitive to large climate variability and the effect of extreme events (Wang et al. 2022; Castellanos et al. 2022), and it is of great importance to understand how well they are reproduced in CMIP models. Our studies imply that, on an average level, the included CMIP6 models failed to capture the realistic pattern in those regions.

The three-signal analysis, which additionally considers GHGs and AERs alongside NAT forcings, is displayed in Fig. 4. The results showed a consistent attributable effect from GHG across all regions, except for South America and Oceania. Notably, several regions exhibited scaling factors significantly below 1, indicating that the simulated response to GHG might be overestimated when compared to the actual observations. Meanwhile, AER and NAT forcings did not show detectable effects in most regions, aligning with observations by Gillett et al. (2021) that NAT forcing is less detectable in CMIP6 than in CMIP5 simulations. As for those regions standing out in the two-signal analysis, specifically NEN, SAM, RAR, and TIB, which are sensitive to climate variability, the detection and attribution conclusions became more unreliable in the three-signal study. Compared to the two-signal analysis, the responses to external forcings GHG and AER are less accurately captured. This is particularly evident in the SAM region, where none of the three forcings were detected. These findings reaffirm that the model simulations did not match the observed pattern of individual forcings.

5. Discussion

The reliability of detection and attribution analysis in climate science, especially when using optimal fingerprints, heavily relies on the precision of the confidence intervals for scaling factors. Recent studies, however, have raised concerns about the adequacy of this method in providing confidence intervals with desired coverage rates (DelSole et al. 2019; Li et al. 2021). This shortcoming could potentially lead to erroneous conclusions in existing research. To address this, we applied the EE approach recently proposed by Ma et al. (2023) to the latest HadCRUT5 observational data and CMIP6 model simulations, performing detection and attribution analyses at both global and regional scales. Here, we revisit the conclusions drawn from previous detection and attribution analyses on global temperature. Additionally, we also conducted detection and attribution analyses of mean temperature on regional scales for all AR6 regions.

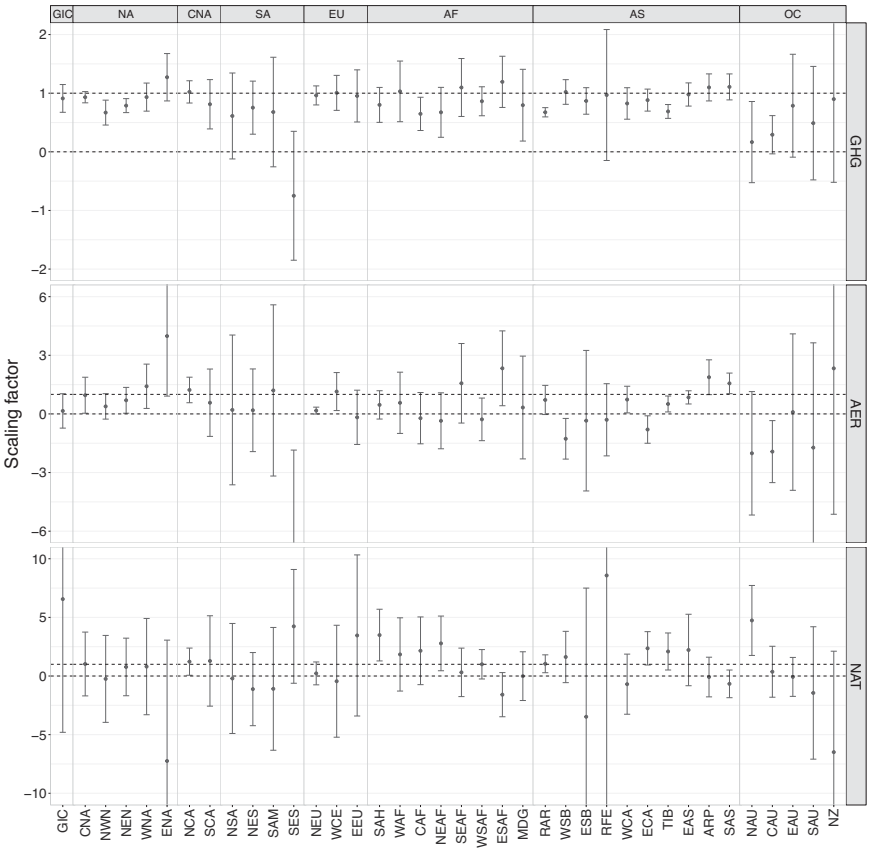

FIG. 4. Estimated signal scaling factors required to best match observed 1950–2020 annual-mean temperature for different regional domains. (from top to bottom) The three panels show results for the three-signal analysis. 90% confidence intervals are constructed from the EE approach. The longest few intervals for the AER and NAT scaling factors are cropped to improve visualization.

We confirmed that the main conclusions of Gillett et al. (2021) on global temperature that was based on the ROF method remain valid despite the undercoverage of the ROF method. In our two-signal and three-signal analyses for the global mean temperature, ANT, GHG, and AER forcings are consistently detected, while natural forcing remains undetected. We note, however, that the ROF-based detection framework can be affected by the details of data analyses, such as the dimensionality of data being used. Gillett et al. (2021) only considered a temporal variation of the global area-weighted 5-yr mean temperature, and their conclusions are similar to ours, in which we also considered the spatial distribution of the mean temperature, but our ROF-based analysis of global temperature also took both space and time into consideration and produced different results from that of the EE method. Thus, it appears that the underestimated uncertainties and the lower efficiency of the method used in Gillett et al. (2021) tune the length of the confidence interval in divergent directions and may have played a crucial role in producing seemingly proper conclusions but with less statistical clarifications. One should note this is only one data analysis, so we cannot conclude the confidence intervals from the EE approach are more accurate than the other approaches based on the results solely. However, as elaborated in the extensive simulation studies conducted by Ma et al. (2023), the results by the EE approach are more reliable and efficient. Thus, we claim the conclusions from the EE approach should be more convincing.

Estimates of the human-induced forcings attributable to warming relative to the preindustrial period are also of great importance. It is notable that our 90% confidence intervals for the contributions from the ANT, GHG, and AER forcings, from 1.01° to 1.25°C, from 1.70° to 2.11°C, and from −0.89° to −0.42°C, respectively, are substantially shorter than their counterparts in Gillett et al. (2021) and IPCC AR6. This is probably due to the improved efficiency of the EE approach. Based on the characteristics of the ROF and the alternative EE framework, our results might give a more precise and fair picture of the influences of human-induced changes in greenhouse gases and aerosols.

The detection and attribution analyses using CMIP6 data on different regional scales have not been explored in the previous literature. It is notable that our analyses reveal that ANT forcing and GHG forcing are detected in most regions, with the exception of regions like South Asia and Oceania.

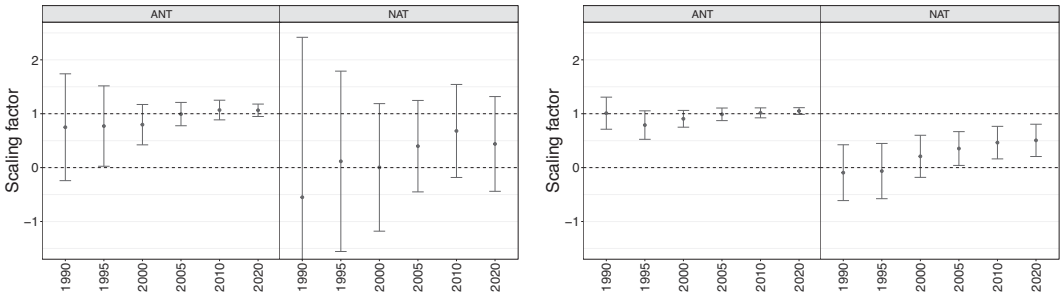

FIG. 5. Estimated signal scaling factors and corresponding 90% confidence intervals to best match annual-mean temperature over various time periods commencing in 1951 on a global scale. The *x* axis represents the hypothetical cutoff points. (from left to right) The two panels show results for the two-signal analysis of ANT and NAT forcings with EE and TS approaches, respectively. The longest interval for the NAT scaling factors is cropped to improve visualization.

However, the AER and NAT forcings are less detectable on the regional scales, which is consistent with the statement of Gillett et al. (2021) that the aerosol and natural forcings are hard to detect on CMIP6. Additionally, it is also notable that in certain regional scales, such as northeastern (NE) North America, Central America, and some regions in Asia, the multimodel average tends to overestimate the response to the GHG forcing with smaller estimated scaling factors compared to unity, likely attributed to the large biases and uncertainties in CMIP6 simulations for those regions. Further studies on how well the climate model simulated the responses to individual forcings at the relevant regions might be of interest.

Given the crucial role detection and attribution analyses have played in the successive IPCC assessment reports, it is interesting to ask if changes in global temperature could have been detected and attributed to human influence at the time of the IPCC assessment, with observational records, climate models, and statistical methodologies as advanced as available today. Here, we conducted detection and attribution analyses with the aim to separate the responses from ANT and NAT forcings across different periods that start from 1951 and end in the year of the assessments, using the HadCRUT5 and CMIP6 model simulations with the EE approach and the TS approach. The results are presented in Fig. 5. Notably, at the time of the first assessment report that stated "the unequivocal detection of the enhanced greenhouse effect from observations is not likely" (IPCC 1990), the ANT signal was also not detectable based on the EE approach. The approach marginally detected the ANT signal at the time of the second assessment that stated "the balance of evidence suggests a discernible human influence on global climate" (IPCC 1996). Starting from the time of the third assessment report, with the increase in the sample size and signal strength, the EE approach robustly detects the ANT signal and attributes the observed changes in global temperature to anthropogenic forcing, with ever-increasing confidence as demonstrated by the reduced size of the confidence interval of the scaling factor corresponding to successive assessments. But, the response to NAT forcing was not detected for any period due to its weak signals. If optimal fingerprinting with a two-sample approach (i.e., TS approach) was applied on identical datasets, we would robustly detect the ANT signal even for the early periods 1951–90 and 1951–95. Such a detection would be most likely an artifact of the analyses as the coverage rate is greatly reduced with shorter time periods. Additionally, the TS method would also detect the response to NAT forcing, which could also be an artifact as the coverage rate is very low for weak signals.

Our analysis underscores the EE approach's potential as an effective alternative to ROF-based methods. Nevertheless, this approach simplifies the multimodel average calculation for external forcings' responses and covariance matrices by not accounting for variations among different climate models. This simplification overlooks the distinct qualities inherent in each model, as highlighted by Gillett et al. (2021) in their single-model analyses. A more comprehensive model could integrate a random effect to reflect the heterogeneity in the simulated fingerprints across various climate models, suggesting an area for future enhancement of the EE approach. For future analyses, the consideration of model-specific or forcing-specific scale parameters, when multiple climate models are analyzed, would improve the method's applicability.

Acknowledgments. We are grateful for the feedback from the two reviewers and the editor.

Data availability statement. The R code for the EE method is available in the R package dacc published on CRAN (https://cran.r-project.org/web/packages/dacc/index.html). The gridded data we used are also available in the dacc package. The data for the numerical studies are available online: HadCRUT5 at https://www.metoffice.gov.uk/hadobs/hadcrut5/ and CMIP6 climate model simulations at https://pcmdi.llnl.gov/CMIP6/. The selected historical and preindustrial runs are listed in the tables of the main text.

APPENDIX

Review of EE Approach

The method of Ma et al. (2023) is developed based on estimation equation theory, which requires less distributional

assumption and is more robust than the likelihood-based methods. In this section, we adopt basic notations from Ma et al. (2023) and illustrate the technical details of the EE approach.

We consider a dataset with T time periods and S spatial regions or sites. For time $t = 1, \ldots, T$ and site $s = 1, \ldots, S$, we denote the observed climate variable (e.g., annual average temperature) as Y_{ts}, the true but unobserved fingerprint of external forcing j as X_{tsj}, and its observed contaminated version as $\tilde{X}_{tsj}$ with m_j being the number of simulations in the ensemble. A set of control runs, which will be used to estimate the pattern of internal climate variability, is denoted as $\{\boldsymbol{\epsilon}^{(1)}, \ldots, \boldsymbol{\epsilon}^{(L)}\}$, each with dimension spatiotemporal (ST). Denote $Y_t = (Y_{t1},\ldots,Y_{ts})^\top$, $X_{tj} = (X_{t1j},\ldots,X_{tSj})^\top$, and $X_t = (X_{t1}, \ldots, X_{tJ})$. The terms $\tilde{X}_{tj}$ and $\tilde{X}_t$ admit similar forms as X_{tj} and X_t. The linear regression model for OF is written as follows:

$$Y_t = X_t\beta + \boldsymbol{\epsilon}_t, \quad \text{and} \quad \tilde{X}_{tj} = X_{tj} + \nu_{tj},$$

where $\boldsymbol{\epsilon}_t = (\epsilon_{t1},\ldots,\epsilon_{tS})^\top$.

Ma et al. (2023) assume that the regression error $\boldsymbol{\epsilon}_t$ and measurement errors $\boldsymbol{\nu}_{tj}$ have mean zero and covariance matrices $\boldsymbol{\Sigma}_t$ and $\boldsymbol{\Omega}_{tj}$, and $\boldsymbol{\Omega}_{tj} = a\boldsymbol{\Sigma}_{tj}/m_j$, whereas traditional OF assumes $a = 1$ and requires checking the residual consistency (Allen and Tett 1999). The estimator of β is not affected by the scale factor a (Ma et al. 2023). However, a does influence the construction of the confidence interval. Additionally, the variation among multiple models is not accounted for in the current EE framework. Future research should focus on modeling the discrepancies among different climate models to enhance the robustness of the approach. A set of corrected estimating equations has been constructed as follows:

$$\frac{1}{T}\sum_{t=1}^{T} G_t(\beta; \boldsymbol{\Sigma}_t) = 0,$$

where $G_t(\beta; \boldsymbol{\Sigma}_t) = \tilde{X}_t^\top\Sigma_t^{-1}(Y_t - \tilde{X}_t\beta) + aS\text{diag}(m_1^{-1}, \ldots, m_J^{-1})\beta$. Then, an unbiased estimator of β can be obtained by solving this equation with $\boldsymbol{\Sigma}_t$ being estimated from control runs $\{\boldsymbol{\epsilon}^{(1)},\ldots,\boldsymbol{\epsilon}^{(L)}\}$ under the assumption that the covariance of control runs shares the same structure as $\boldsymbol{\Sigma}_t$ with only scale difference a. That is, with $\hat{\boldsymbol{\Psi}}_+$ representing the pooled estimates of $\boldsymbol{\Psi}_t$ values, the covariance matrix of the control runs $\boldsymbol{\epsilon}_t$ is

$$\hat{\beta}_T = \frac{1}{T}A_T\sum_{t=1}^{T}\tilde{X}_t\hat{\Psi}_+^{-1}Y_t, \quad \text{and}$$

$$A_T = \left[\frac{1}{T}\sum_{t=1}^{T}\tilde{X}_t^\top\hat{\Psi}_+^{-1}\tilde{X}_t - S\text{diag}\left(\frac{1}{m_1},\ldots,\frac{1}{m_J}\right)\right]^{-1}.$$

More details of obtaining $\hat{\boldsymbol{\Psi}}_+$ can be found in Ma et al. (2023, section 2b).

Based on the theory of estimating equations, $\hat{\beta}_T$ is approximately unbiased with a large number of time points T; more importantly, the method of Ma et al. (2023) does not make any distributional assumptions, which makes it more robust and adaptive. Further, one can construct the confidence interval for β based on the normal approximation as $T \to \infty$:

$$\sqrt{T}(\hat{\beta}_T - \beta) \to N(0, ABA^\top),$$

where $A = \lim_{t\to\infty}A_T$, $B = \lim_{T\to\infty}B_T$, and $B_T = \text{cov}\left\{T^{-1/2}\sum_{t=1}^{T}G_t(\beta; \hat{\boldsymbol{\Sigma}}_+)\right\}$. In practice, A can be estimated by A_T, whereas B is hard to estimate due to the unspecified temporal dependence in the data. Thus, a pseudoresidual bootstrap is proposed in Ma et al. (2023) in estimating B only, rather than the entire asymptotic variance. This algorithm utilizes control runs in place of bootstrapped residuals while preserving the spatial and temporal dependence. We would like to emphasize that the pseudobootstrap procedure employed in the EE approach deviates from standard bootstrap methods. The primary challenge lies in generating bootstrap replicates of the data that preserve temporal dependence, given that the off-diagonal blocks of $\boldsymbol{\Sigma}$ are not explicitly specified. Although block bootstrap techniques do not require a specification of temporal dependence, they are unsuitable for our detection and attribution (D&A) analysis due to the limited temporal dimension. The innovation of our procedure exploits the fact that control runs exhibit the same temporal structure, up to the scaling parameter a. By applying appropriate scaling, one can generate bootstrap replicates of the residuals that maintain the temporal dependence present in the control runs. Besides, Ma et al. (2023) also described diagnosis methods for the proposed method regarding the scale parameter a. In the application to the annual-mean near-surface air temperature at the global, continental, and subcontinental scales based on the CanESM5 climate model simulations, it has been revealed that the scale parameter a is statistically different from 1 in many regions, and the proposed method can provide unbiased estimators and valid confidence intervals.

In this paper, we have also examined the scale parameter a of the EE method. Both the two-signal and three-signal analyses suggest that the scale parameter remains constant ($a = 1$) across different ensembles with confidence intervals being (0.73, 1.20) and (0.75, 1.21), respectively, which is consistent with the common assumption of the optimal fingerprinting method in Gillett et al. (2021). Since, on the global scale, different climate ensemble models may have different scale parameters, after taking the average, the effect of scale parameters diminished, and the overall average scale parameters are equal to 1. Nonetheless, for many of the continental and subcontinental scale analyses, especially for the continental regions South America and Asia, where the responses to the detected forcings are overestimated (the confidence intervals are statistically lower than 1), the conclusions are consistent with the results of Ma et al. (2023), and the scale parameter is statistically different from 1, which suggests further investigations on the climate model simulations of those regions are needed.

REFERENCES

Allen, M. R., and S. F. B. Tett, 1999: Checking for model consistency in optimal fingerprinting. *Climate Dyn.*, **15**, 419–434, https://doi.org/10.1007/s003820050291.

——, and P. A. Stott, 2003: Estimating signal amplitudes in optimal fingerprinting, part I: Theory. *Climate Dyn.*, **21**, 477–491, https://doi.org/10.1007/s00382-003-0313-9.

Castellanos, E., and Coauthors, 2022: Central and South America. *Climate Change 2022: Impacts, Adaptation and Vulnerability*, H.-O. Pörtner et al., Eds., Cambridge University Press, 1689–1816.

DelSole, T., L. Trenary, X. Yan, and M. K. Tippett, 2019: Confidence intervals in optimal fingerprinting. *Climate Dyn.*, **52**, 4111–4126, https://doi.org/10.1007/s00382-018-4356-3.

Eyring, V., S. Bony, G. A. Meehl, C. A. Senior, B. Stevens, R. J. Stouffer, and K. E. Taylor, 2016: Overview of the Coupled Model Intercomparison Project Phase 6 (CMIP6) experimental design and organization. *Geosci. Model Dev.*, **9**, 1937–1958, https://doi.org/10.5194/gmd-9-1937-2016.

——, and Coauthors, 2021: Human influence on the climate system. *Climate Change 2021: The Physical Science Basis*, V. Masson-Delmotte et al., Eds., Cambridge University Press, 423–552.

Gillett, N. P., and Coauthors, 2021: Constraining human contributions to observed warming since the pre-industrial period. *Nat. Climate Change*, **11**, 207–212, https://doi.org/10.1038/s41558-020-00965-9.

Gutiérrez, J. M., and Coauthors, 2021: Atlas. *Climate Change 2021: The Physical Science Basis*, V. Masson-Delmotte et al., Eds., Cambridge University Press, 1927–2058.

Hannart, A., 2016: Integrated optimal fingerprinting: Method description and illustration. *J. Climate*, **29**, 1977–1998, https://doi.org/10.1175/JCLI-D-14-00124.1.

——, A. Ribes, and P. Naveau, 2014: Optimal fingerprinting under multiple sources of uncertainty. *Geophys. Res. Lett.*, **41**, 1261–1268, https://doi.org/10.1002/2013GL058653.

Hasselmann, K., 1997: Multi-pattern fingerprint method for detection and attribution of climate change. *Climate Dyn.*, **13**, 601–611, https://doi.org/10.1007/s003820050185.

Hegerl, G. C., H. von Storch, K. Hasselmann, B. D. Santer, U. Cubasch, and P. D. Jones, 1996: Detecting greenhouse-gas-induced climate change with an optimal fingerprint method. *J. Climate*, **9**, 2281–2306, https://doi.org/10.1175/1520-0442(1996)009<2281:DGGICC>2.0.CO;2.

——, O. Hoegh-Guldberg, G. Casassa, M. P. Hoerling, R. S. Kovats, C. Parmesan, D. W. Pierce, and P. A. Stott, 2010: Good practice guidance paper on detection and attribution related to anthropogenic climate change. *Meeting Report of the Intergovernmental Panel on Climate Change Expert Meeting on Detection and Attribution of Anthropogenic Climate Change*, T. F. Stocker et al, Eds., 8 pp., https://www.ipcc.ch/site/assets/uploads/2018/08/ipcc_good_practice_guidance_paper_anthropogenic.pdf.

IPCC, 1990: Climate change. *The IPCC Scientific Assessment Contribution of Working Group I to the First Assessment Report of the Intergovernmental Panel on Climate Change*, J. Houghton, G. J. Jenkins, and J. J. Ephraums, Eds., Cambridge University Press, 365.

——, 1996: *Climate Change 1995: The Science of Climate Change*. J. Houghton et al., Eds., Cambridge University Press, 588 pp.

Iturbide, M., and Coauthors, 2020: An update of IPCC climate reference regions for subcontinental analysis of climate model data: Definition and aggregated datasets. *Earth Syst. Sci. Data*, **12**, 2959–2970, https://doi.org/10.5194/essd-12-2959-2020.

Ledoit, O., and M. Wolf, 2004: A well-conditioned estimator for large-dimensional covariance matrices. *J. Multivar. Anal.*, **88**, 365–411, https://doi.org/10.1016/S0047-259X(03)00096-4.

Li, Y., K. Chen, J. Yan, and X. Zhang, 2021: Uncertainty in optimal fingerprinting is underestimated. *Environ. Res. Lett.*, **16**, 084043, https://doi.org/10.1088/1748-9326/ac14ee.

——, ——, and ——, 2023a: *dacc: Detection and Attribution Analysis of Climate Change,* version 0.0-3. R package, https://CRAN.R-project.org/package=dacc.

——, ——, ——, and X. Zhang, 2023b: Regularized fingerprinting in detection and attribution of climate change with weight matrix optimizing the efficiency in scaling factor estimation. *Ann. Appl. Stat.*, **17**, 225–239, https://doi.org/10.1214/22-AOAS1624.

Ma, S., T. Wang, J. Yan, and X. Zhang, 2023: Optimal fingerprinting with estimating equations. *J. Climate*, **36**, 7109–7122, https://doi.org/10.1175/JCLI-D-22-0681.1.

Morice, C. P., J. J. Kennedy, N. A. Rayner, and P. D. Jones, 2012: Quantifying uncertainties in global and regional temperature change using an ensemble of observational estimates: The HadCRUT4 data set. *J. Geophys. Res.*, **117**, D08101, https://doi.org/10.1029/2011JD017187.

——, and Coauthors, 2021: An updated assessment of near-surface temperature change from 1850: The HadCRUT5 data set. *J. Geophys. Res. Atmos.*, **126**, e2019JD032 361, https://doi.org/10.1029/2019JD032361.

Pesta, M., 2013: Total least squares and bootstrapping with applications in calibration. *Statistics*, **47**, 966–991, https://doi.org/10.1080/02331888.2012.658806.

Ribes, A., J.-M. Azaïs, and S. Planton, 2009: Adaptation of the optimal fingerprint method for climate change detection using a well-conditioned covariance matrix estimate. *Climate Dyn.*, **33**, 707–722, https://doi.org/10.1007/s00382-009-0561-4.

——, S. Planton, and L. Terray, 2013: Application of regularised optimal fingerprinting to attribution. Part I: Method, properties and idealised analysis. *Climate Dyn.*, **41**, 2817–2836, https://doi.org/10.1007/s00382-013-1735-7.

Swart, N. C., and Coauthors, 2019: The Canadian Earth System Model version 5 (CANESM5 0.3). *Geosci. Model Dev.*, **12**, 4823–4873, https://doi.org/10.5194/gmd-12-4823-2019.

Tett, S. F. B., and Coauthors, 2002: Estimation of natural and anthropogenic contributions to twentieth century temperature change. *J. Geophys. Res.*, **107**, 4306, https://doi.org/10.1029/2000JD000028.

Wan, H., X. Zhang, and F. Zwiers, 2019: Human influence on Canadian temperatures. *Climate Dyn.*, **52**, 479–494, https://doi.org/10.1007/s00382-018-4145-z.

Wang, X., and Coauthors, 2022: Contrasting characteristics, changes, and linkages of permafrost between the Arctic and the Third Pole. *Earth-Sci. Rev.*, **230**, 104042, https://doi.org/10.1016/j.earscirev.2022.104042.

Zhang, X., F. W. Zwiers, and P. A. Stott, 2006: Multimodel multisignal climate change detection at regional scale. *J. Climate*, **19**, 4294–4307, https://doi.org/10.1175/JCLI3851.1.